

## The Mesoscale Characteristics of Tropical Oceanic Precipitation during Kelvin and Mixed Rossby–Gravity Wave Events

CHRISTOPHER T. HOLDER AND SANDRA E. YUTER

*North Carolina State University, Raleigh, North Carolina*

ADAM H. SOBEL

*Columbia University, New York, New York*

ANANTHA R. AIYYER

*North Carolina State University, Raleigh, North Carolina*

(Manuscript received 15 August 2007, in final form 31 December 2007)

### ABSTRACT

Precipitation structures within Kelvin and mixed Rossby–gravity (MRG) wave troughs near Kwajalein Atoll during the 1999–2003 rainy seasons are analyzed using three-dimensional ground-based radar data and upper-air sounding data. Consistent with previous work, wave troughs are preferred locations for precipitation and typically yield 1.3 times more rain area compared to the overall rainy season climatology.

Although the contiguous areas of cold cloudiness associated with tropical wave troughs are large and long lived, the underlying precipitation structure is most frequently small, isolated convection from mixed-phase clouds. This mismatch in instantaneous cold cloudiness area versus radar-observed precipitation area indicates differences in the rate and nature of evolution between the mesoscale anvil cloud and the underlying precipitating portion of the cloud.

Mesoscale convective systems (MCSs) were identified during portions of 32 of the 39 wave trough events examined. Convective cells are frequently embedded within stratiform regions. Reflectivity holes or pores in contiguous radar echo have been frequently observed in other regions but are quantified for the first time in this study. Based on characteristics such as total size of precipitating area and occurrence of convective lines, MCSs within Kelvin troughs are slightly more organized than those occurring within MRG troughs.

Similar to the west Pacific warm pool region, there is a well-defined separation between observed and unobserved stratiform area fraction and convective precipitation area, each as a function of total precipitation area. At precipitation area sizes near 40% of the radar domain, the maximum observed convective area changes from increasing to decreasing with increasing precipitation area. The maximum observed convective precipitation area occupied ~20% of the radar domain. These characteristics suggest that the atmosphere in the west Pacific can sustain a limited area of updrafts capable of supporting precipitation growth by collision/coalescence and riming.

### 1. Introduction

Equatorial waves account for a significant portion of the variance in the tropical outgoing longwave radiation (OLR) spectrum (Wheeler and Kiladis 1999; Wheeler et al. 2000; Roundy and Frank 2004). Since the theoretical studies by Matsuno (1966), Lindzen (1967),

and Lindzen and Matsuno (1968), the existence, origin, large-scale properties, and convective coupling of equatorial waves have been investigated using reanalysis, satellite observations, and upper-air soundings (e.g., Hendon and Liebmann 1991; Dunkerton 1993; Dunkerton and Baldwin 1995; Pires et al. 1997). The Wheeler and Kiladis (1999) satellite wavenumber–frequency analysis used theoretical wave properties and long-term OLR data. Subsequent studies (e.g., Wheeler et al. 2000; Straub and Kiladis 2002; Straub and Kiladis 2003a,b; Roundy and Frank 2004) analyzed large-scale

---

*Corresponding author address:* Dr. Sandra Yuter, North Carolina State University, Raleigh, NC 27695.  
E-mail: seyuter@ncsu.edu

spatiotemporal wave variability, structure, and associated large-scale convection using the Wheeler and Kiladis (1999) methodology.

Complex global cloud-resolving models are now beginning to reproduce equatorial waves and tropical multiscale interactions (e.g., Grabowski 2003; Randall et al. 2003; Grabowski 2004; Khairoutdinov et al. 2005; Kuang et al. 2005; Ziemiański et al. 2005; Suzuki et al. 2006), but many models do so rather poorly (Majda et al. 2004; Slingo et al. 2007; Yang et al. 2007). Better knowledge of the synoptic- and mesoscale structures of convectively coupled waves would be useful for evaluating simulations of waves and of tropical deep convection in general. Houze et al. (2000), for example, investigated the characteristics of large convective systems within Kelvin waves over the west Pacific warm pool during the Tropical Ocean Global Atmosphere Coupled Ocean–Atmosphere Response Experiment (TOGA COARE; Webster and Lukas 1992). They found very different momentum feedbacks within these large systems depending on their spatial scale and dynamics, which highlights the importance of understanding mesoscale precipitation characteristics of tropical deep convection in order to accurately evaluate scale interactions.

We address the largely uninvestigated mesoscale characteristics of precipitation coupled with Kelvin and mixed Rossby–gravity (MRG) waves. Kelvin and MRG waves explain a significant percentage of tropical synoptic OLR variance (Roundy and Frank 2004). Kwajalein Atoll (8.7°N 167.7°E, Republic of the Marshall Islands) was the site of a major field experiment in 1999, the Kwajalein Experiment (KWAJEX; Yuter et al. 2005), and is one of the few open-ocean tropical Pacific locations with a multiyear weather radar dataset.

This study builds on that of Swann et al. (2006, hereafter S06). S06 examined mesoscale precipitation characteristics during large Kwajalein rain events coincident with significant Kelvin or MRG wave amplitude—that is, significant wave troughs or ridges, as evidenced by OLR maxima and minima, respectively. We refer to the S06 dataset as “rain event–centric.”

In S06, comparison of contoured frequency-by-altitude diagrams (CFADs; Yuter and Houze 1995) of accumulated reflectivities for their rain event–centric Kelvin and MRG events showed that modal reflectivities for Kelvin events were slightly weaker than those for MRG events. S06 interpreted the weaker reflectivities to imply larger mean stratiform precipitation areas in Kelvin waves. In turn, larger stratiform areas suggest enhanced mesoscale precipitation organization during some Kelvin events compared to MRG.

In this study, we separate the rain event–centric radar reflectivities into convective and stratiform regions to verify that S06’s Kelvin events contain larger stratiform precipitation areas than their MRG events. Whereas S06 focused on large precipitating structures within both wave troughs and wave ridges, in this study we examine all precipitating structures within wave troughs. We refer to our dataset as “trough event–centric.” We also utilize an array of statistical analyses on operational weather radar data beyond the preliminary analyses performed in S06. Most of these analyses are objective and ideal for reproducibility with other datasets, and some techniques are used here for perhaps the first time in their current form.

S06’s and our wave event–defining methodologies have some arbitrariness and are both arguably valid ways of examining wave-coupled convection. Our wave event definitions and differences with S06 are detailed in section 2a. Comparing the results of our methodology with those of S06 tests the robustness of the results. Furthermore, the multiyear operational weather radar dataset at Kwajalein allows us to characterize the general properties of precipitating structures near Kwajalein and to compare these typical structures to those within Kelvin and MRG wave troughs. While it is beyond the scope of this study to extend our detailed radar analyses to the entire 1999–2003 dataset of three-dimensional radar volumes, our trough event–centric dataset and the S06 rain event–centric dataset together are a large subsample of three-dimensional Kwajalein precipitation data. The S06 rain event–centric dataset represents large rain events and our trough event–centric dataset represents large-scale environments that should favor convection based on anomalously negative OLR data. Considering the S06 rain-centric wave events and our trough-centric wave events together, we examine roughly 17% of the collected three-dimensional radar volumes during our time period and 30% of the multiyear cumulative rain area [see section 2b(1) for more information on the representativeness of these datasets]. We also use the entire three-year rainy season dataset of two-dimensional long-range radar scans (~800 days) to describe the typical sizes of Kwajalein rain areas.

This study uses Kwajalein radar data to address several questions: Which results from S06 are robust to the change in wave event definition? Are there other significant differences between the Kelvin and MRG mesoscale precipitation structures, besides those found in the brief S06 study? Assuming our data samples are representative, what are the general mesoscale precipitation structure characteristics near Kwajalein? How do

TABLE 1. The wave event–defining methodologies of this study and of the S06 study, along with the number of wave events and event days defined using these methods. S06 also employed some smoothing parameters that are discussed in their study. S06 used satellite scans at 24-h resolution in their OLR filtering, whereas we used 12-h resolution, so many of their events were longer than ours.

	Our trough events	S06 wave events
Period	Jul–Dec 1999–2003	Jul–Dec 1999–2001 Jul–Sep 2002
OLR filtering spectral windows	Fig. 6 of Wheeler and Kiladis (1999)	Kelvin: Fig. 6 of Straub and Kiladis (2002) MRG: Fig. 3 of Wheeler and Kiladis (1999)
OLR spatial averaging domain	5°–12.5°N, 162.5°–170°E	0°–15°N, 165°–170°E
Wave amplitude requirements	Negative, $\geq 1.5\sigma$ for $\geq 24$ h	Positive or negative, $\geq 2\sigma$
Rain area requirements	None	$\geq 2\sigma$
No. of wave events	23 Kelvin 16 MRG	22 Kelvin 22 MRG
No. of wave event days	25.5 Kelvin 16 MRG	52 Kelvin 48 MRG

these characteristics compare to those found in other studies of other tropical oceanic regions?

## 2. Data and methodology

### a. Identifying Kelvin and MRG waves

Kelvin and MRG waves are identified with the Wheeler and Kiladis (1999) OLR spectral analysis method. Wave-filtered OLR is calculated from twice-daily (0600 and 1800 UTC) National Oceanic and Atmospheric Administration (NOAA) polar-orbiting satellite data interpolated as in Liebmann and Smith (1996). We require that filtered anomalies retain the equatorial symmetry properties described in linear theory: an equatorially symmetric Kelvin OLR structure, antisymmetric for MRG. Removing symmetry constraints, as in some previous studies (e.g., Straub and Kiladis 2002; Straub and Kiladis 2003b; Roundy and Frank 2004), generally does not alter our wave events significantly.

Details of the event-defining methodologies of our study and of S06 are highlighted in Table 1. For our study, filtered OLR fields for each wave type are spatially averaged across a  $7.5^\circ \times 7.5^\circ$  grid centered over Kwajalein. During the rainy seasons (July–December) of 1999–2003, wave trough events are periods of at least 24 h where this average negative wave-filtered OLR anomaly is at least 1.5 standard deviations ( $\sigma$ ) larger than the mean anomaly calculated from the 1997–2005 dataset. This methodology focuses specifically on wave troughs and identifies 23 Kelvin trough events and 16 MRG trough events. Larger values of  $\sigma$  identify too few events for our results to be robust, smaller values result in many weaker trough events. The composite wave-filtered and raw OLR anomalies for our trough events are shown in Fig. 1 for days  $-2$ ,  $0$ , and  $+2$ . Strong negative wave-filtered OLR anomalies pass near Kwa-

jalein at day 0, which is also visible in the raw OLR data.

Twice-daily upper-air soundings were obtained from the National Climatic Data Center Integrated Global Radiosonde Archive (available online at <http://www.ncdc.noaa.gov/oa/climate/igra/index.php>) and interpolated to finer vertical resolution as in Sobel et al. (2004). The frequency distributions of vertical wind shear direction within the 1000–700-hPa layer during Kelvin and MRG waves are generally similar to the distributions of the entire 1999–2003 rainy season dataset (Fig. 2). There is a higher frequency of shear speeds  $>6$   $\text{m s}^{-1}$  during Kelvin troughs than during MRG troughs and typical Kwajalein observations (Fig. 2), indicating the propensity of stronger OLR anomaly amplitudes during Kelvin waves than MRG waves, which is also seen in Fig. 1.

S06 identified rain areas exceeding the Kwajalein mean area by  $2\sigma$  that were coincident with positive and negative wave-filtered OLR anomalies also exceeding  $2\sigma$  (Table 1). S06 identified 22 Kelvin wave events and 22 MRG wave events. Examining both wave ridges and troughs allowed for wave-related convection possibly lagging or leading the trough due to dynamics of individual storms. This is a rain event–centric approach, compared to trough event–centric in our study. A total of 15 of 75 S06 Kelvin wave event days and 5 of 48 S06 MRG wave event days correspond to our Kelvin and MRG trough event days. Because the S06 wave event definition was not conditioned on the presence of strong wave troughs, many S06 wave events contained wave ridges and some events spanned nearly an entire wavelength.

### b. Radar data

#### 1) KWAJALEIN RADAR

Table 1 of Houze et al. (2004) provides the characteristics of the Kwajalein operational S-band radar.

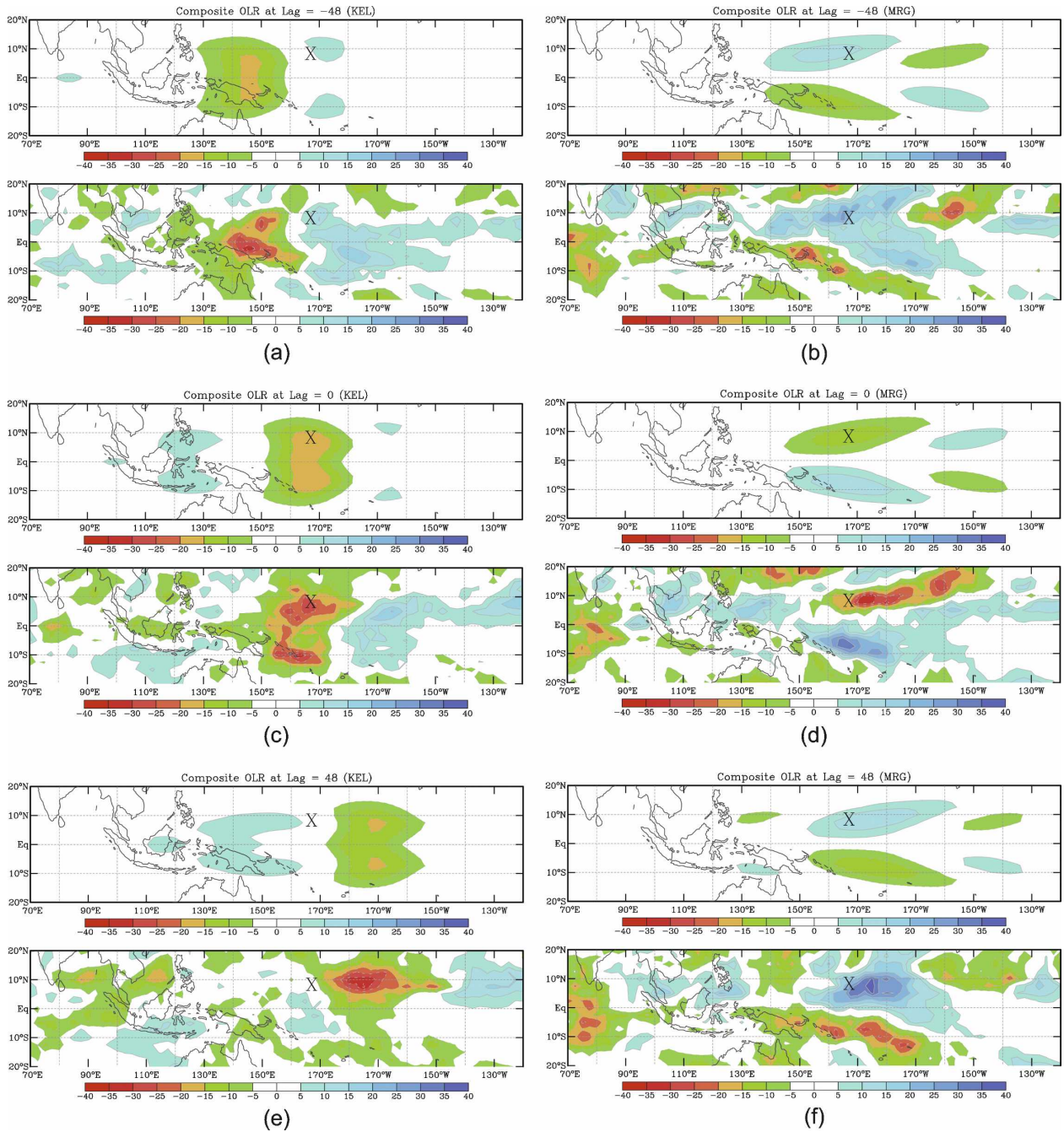


FIG. 1. (a), (c), (e) Kelvin and (b), (d), (f) MRG OLR anomaly data ( $W m^{-2}$ ). Throughout, the (top of each) wave-filtered OLR anomaly data and the (bottom of each) raw OLR anomaly data are shown. Lag times are given as (a), (b)  $-48$ ; (c), (d)  $0$ ; and (e), (f)  $+48$  h. An X marks the location of Kwajalein.

Three-dimensional radar volumes, completed in 10–12-min intervals, are quality controlled as described in Sobel et al. (2004). Meteorological echoes within about  $15 km \leq radius \leq 157 km$  (scan area  $\sim 76\,730 km^2$ ) are interpolated to a Cartesian grid with 2-km horizontal and vertical grid spacing. Radar calibration corrections

(Table 2) follow Houze et al. (2004). Periods without a specified correction are not calibrated. In total, 3609 radar volumes comprise our Kelvin trough events and 2028 for MRG troughs.

A single-elevation long-range (radius = 240 km, scan area  $\sim 180\,248 km^2$ ) scan follows each volume scan. The

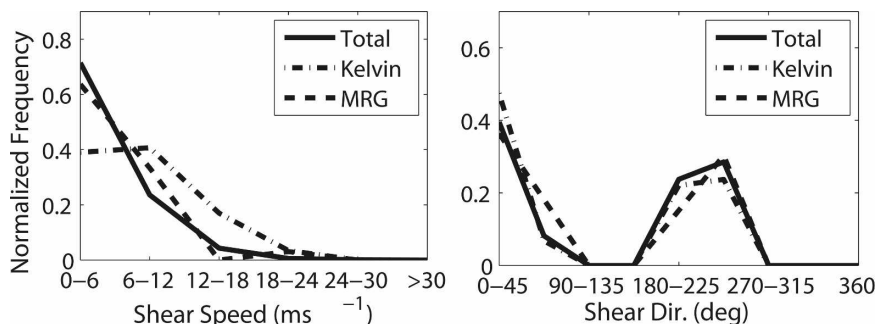


FIG. 2. Normalized frequency distributions of vertical wind shear in the 1000–700-hPa layer (the difference in wind speed and direction between the 1000- and 700-hPa level) for all trough event soundings (Kelvin: 59 soundings, MRG: 33 soundings).

entire rainy season 1999–2003 time series of two-dimensional long-range scans had been previously processed (Yuter et al. 2005). Only three-dimensional radar volumes specific to the wave event times of S06 and this study are processed. We describe “typical” Kwajalein horizontal rain areas using the two-dimensional long-range scan dataset. Early July 1999 and most of October–December 2002 are missing from the long-range dataset because of radar malfunctions. These periods contain three Kelvin trough events (events 1, 15, 16; Fig. 3a) and one MRG trough event (event 15; Fig. 3b).

Expectedly, during trough events, rain areas in long-range scans were generally larger than is typical near Kwajalein (Table 3—note that the differences between wave-specific rain areas and “climatological” precipitation areas are shown in parentheses). On average, trough event-centric rain areas were 1.3 times larger than typical Kwajalein rain areas. During the 1999–2003 rainy seasons, Kelvin and MRG trough events account for 5% of the long-range radar scans (Table 3) and 7% of the cumulative rain area. Together, our trough event-centric dataset and the S06 rain event-centric dataset account for 20% of long-range radar scans and 30% of the cumulative rain area. Less than 1% of all rainy season 1999–2003 long-range radar scans show no precipitation activity, and similarly small percentages are found in our trough event-centric radar subset and in the S06 rain event-centric radar subset.

Reanalyses can often be unreliable across the tropical oceans because of sparse observed data. Using the methods below to analyze three-dimensional radar data, we infer general, relative mesoscale precipitation organization based on the general appearance of MCSs and convective lines as well as the relative sizes of rain areas. Our organizational statistics should be relatively insensitive to sea surface temperature (SST) because the maxima and minima in rainy season SST varied by

only about 0.5°C. There was not a strong correlation between the phase of the El Niño–Southern Oscillation and wave activity or wave event rain areas.

## 2) CONVECTIVE AND STRATIFORM SEPARATION

Convective and stratiform precipitation maps are derived from the interpolated reflectivity fields (2 km in horizontal) for the 0–2-km altitude layer of radar volumes for the rain event-centric and trough event-centric times following the methodology described in Yuter et al. (2005), which is based on an algorithm developed by Steiner et al. (1995). The “this study: best” category of Table B1 from Yuter et al. (2005) specifies convective and stratiform criteria used. Convective cores are pixels whose reflectivities are  $\geq 40$  dBZ or exceed a defined reflectivity difference compared to the average of surrounding pixels within a radius of 11 km. The reflectivity difference used to identify a convective core decreases with increasing background reflectivity. Convective precipitation region radii about these cores are defined based on the magnitude of the reflectivity difference. All other pixels with reflectivity greater than 15 dBZ are considered stratiform precipitation, and radar echo 15 dBZ or less

TABLE 2. Radar calibration corrections applied to the radar volumes of the trough events in this study (following Houze et al. 2004). Some periods of 2001 and all of 2002 and 2003 had no specified calibration correction (denoted here as N/A), so the radar volumes in these periods were not corrected.

Calibration correction	% Radar volumes		
	Kelvin	MRG	Tot
–3 dB	0%	7%	3%
0 dB	18%	30%	22%
+1 dB	13%	0%	8%
+6 dB	19%	19%	19%
N/A (0 dB)	50%	44%	48%

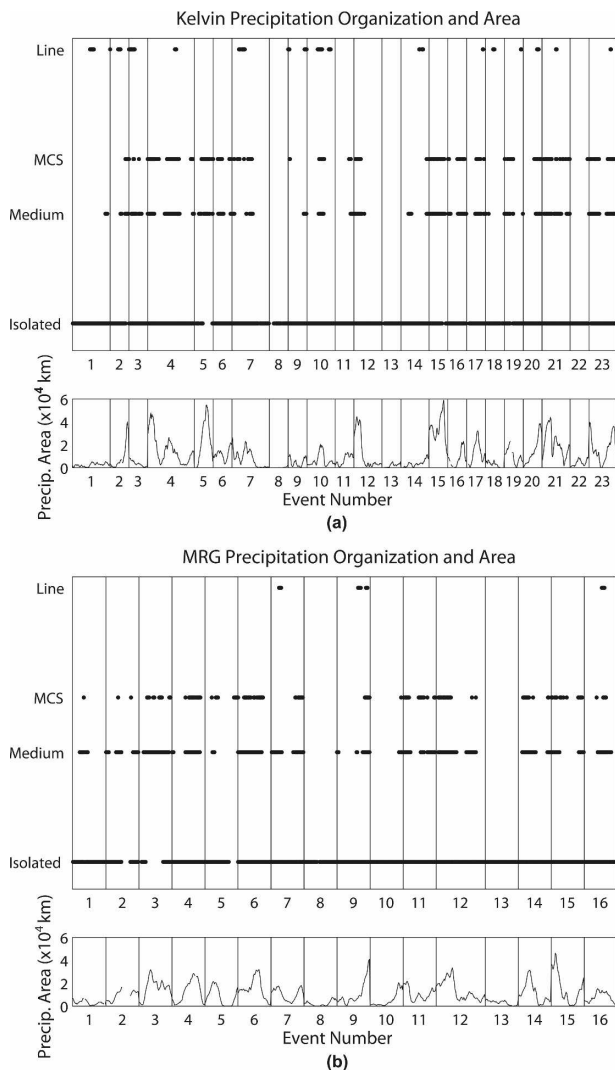


FIG. 3. Horizontal precipitation organization for trough-centric (a) Kelvin radar volumes and (b) MRG volumes, along with observed precipitation areas (bottom of each). Organization is determined visually [section 2b(3)] using the 0–2-km altitude layer of the radar volumes [radius ( $r$ ) = 157 km, domain area ( $A_d$ ) = 76 730 km<sup>2</sup>]; precipitation areas are also extracted at these half-hour intervals. Wave events are separated by vertical lines, and a point is placed at each time for the type(s) of organization seen at that time. Note that these are not continuous time series.

is classified as weak echo. Precipitating areas are defined as the set of pixels of reflectivity exceeding 15 dBZ (rain rates exceeding 0.32 mm h<sup>-1</sup>, Houze et al. 2004). Figure 4 provides two examples of radar reflectivity scans (Figs. 4a,d) and their corresponding convective-stratiform-weak maps (Figs. 4b,e).

### 3) VISUAL ORGANIZATION CLASSIFICATION

We examine convective-stratiform-weak maps (e.g., Figs. 4b,e) at 30-min intervals during trough events.

Similar to previous studies (e.g., Rickenbach and Rutledge 1998; Parker and Johnson 2000), we tabulate statistics for the several organizational categories that are defined below: convective lines, MCSs, medium-sized non-MCS rain areas, and isolated. Multiple organization types can coexist.

Convective lines are at least 100 km long (e.g., Parker and Johnson 2000) and exist for at least 30 min (2 scans when viewing at 30-min intervals) within the radar domain (radius = 157 km). MCSs have rain areas of at least 2500 km<sup>2</sup> and length scales that are at least 100 km (Houze 2004) and no more than twice the width scale. Nine of the 30 identified convective lines developed significant stratiform structures, allowing those lines to meet the size and aspect ratio requirements of an MCS. In all nine cases, the stratiform area trailed the convective line. We classify these nine convective lines with significant trailing stratiform structures solely as MCSs, so that the “line” category only includes lines without significant stratiform structures.

“Medium-sized” contiguous rain areas are at least 2500 km<sup>2</sup> in area with at least three embedded convective cores but do not satisfy MCS length scale requirements. Individual rain areas not fitting the above categories are “isolated.” If less than 10 isolated rain areas totaling less than 900 km<sup>2</sup> rain area coexist with another organization, we do not note coexisting isolated activity.

These various time and space requirements are simple to visually measure and provide clearly defined horizontal organization categories. Only 3% of the 30-min interval Kelvin scans and 2% of 30-min interval MRG scans are missing or showed no activity. The organizational statistics in section 4 are for convectively active radar scans at 30-min intervals unless otherwise noted.

### 4) CONTIGUOUS RAIN AREA “BLOB” ANALYSIS

We use a “blob analysis” algorithm, developed by P. Blossey of the University of Washington (see online at <http://www.atmos.washington.edu/~bloss/blobcount/>), to objectively analyze individual contiguous rain area blobs exceeding 15 dBZ in the 0–2-km altitude layer of trough radar reflectivity volumes. Contiguous pixels above this reflectivity threshold must share at least one full side. This algorithm is similar to one used on satellite data in Nesbitt et al. (2000), and it determines the number, size, shape, spacing, azimuthal orientation, and reflectivity characteristics of blobs. In automating what would otherwise be a time-consuming and more subjective manual task, this algorithm may be easily applied to other regions and to model output to objectively describe rain areas. Figure 4 shows two examples

TABLE 3. Radar echo areas (km<sup>2</sup>) using the long-range radar scans ( $r = 240$  km,  $A_d \equiv 180\,248$  km<sup>2</sup>, 10–12-min frequency) corresponding to quartiles computed from distributions of cumulative area and cumulative frequency. “All” refers to all July–December 1999–2003 scans. Kelvin and MRG areas are for the trough events in this study. Numbers in parentheses show the (wavetype – all) difference. Long-range scans were unavailable for early July 1999 and most of October–December 2002, omitting three Kelvin events and one MRG event from these statistics.

	Cumulative area			
	0.25	0.5	0.75	Maximum achieved tot echo area
All	17 072	31 120	49 728	128 048
Kelvin	23 936 (+6864)	37 392 (+6272)	56 192 (+6464)	90 752
MRG	21 008 (+3936)	32 288 (+1168)	45 600 (–4128)	64 496
	Cumulative frequency			
	0.25	0.5	0.75	Tot No. samples
All	3759	10 191	23 279	88 241
Kelvin	6831 (+3073)	17 023 (+6833)	33 855 (+10 576)	2934
MRG	8207 (+4448)	18 463 (+8272)	31 503 (+8224)	1692

of radar reflectivity scans (Figs. 4a,d) and their corresponding blob analysis maps (Figs. 4c,f).

The blob’s second moment of inertia tensor eigenvalues (Medioni et al. 2000) provide ellipse-fitting ma-

ter and minor axes lengths. The length ratio of minor-to-major axes is the blob’s aspect ratio, and the blob azimuthal orientation is its major axis angle clockwise from north. This ellipse-fitting technique has been used

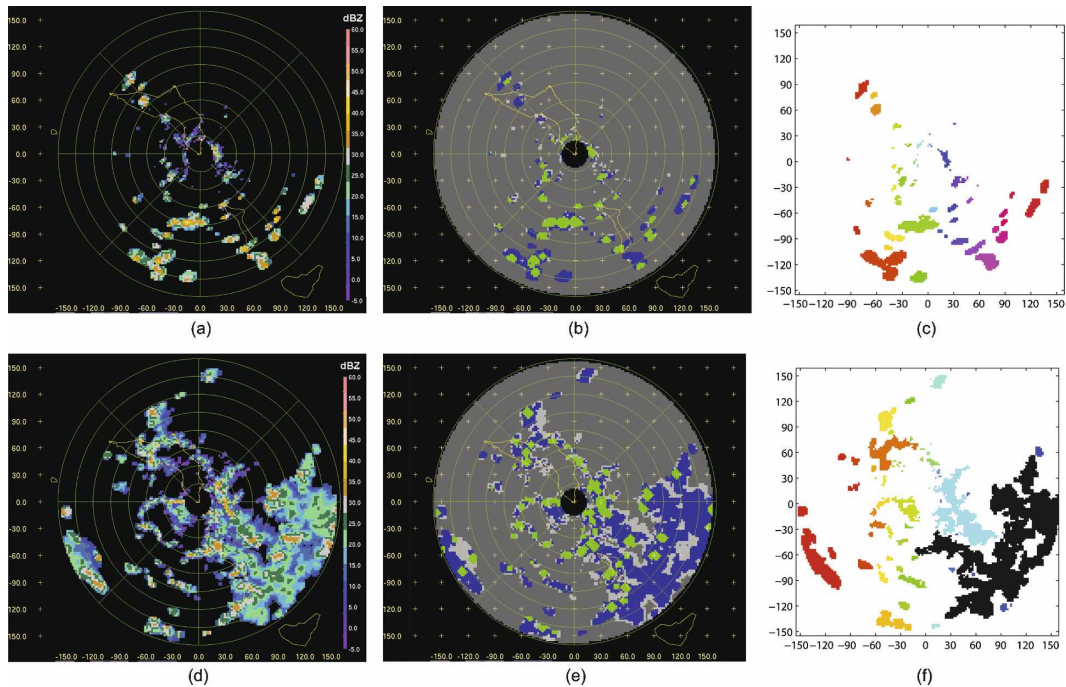


FIG. 4. Example (a), (d) reflectivity; (b), (e) convective–stratiform–weak maps [see section 2b(3)]; and (c), (f) blob detection [see section 2b(4)] representations of two different organizational regimes: (a)–(c) isolated (0549 UTC 13 Dec 2001), and (d)–(f) large rain areas with embedded convection (coexistent with some isolated, 0223 UTC 30 Oct 1999). These images represent data from the 0–2-km altitude layer of the three-dimensional radar volumes ( $r = 157$  km). Distance scales are in km. Convective–stratiform–weak map colors represent weak echo (light gray), stratiform echo (blue), and convective echo (green). Individual colors on the blob detection represent different individual contiguous rain blobs. The dark MCS blob in (f) is referred to in the text for its embedded areas of weak reflectivity (white space within the dark blob), which we call porosity [see sections 2b(5) and the subsection in 4b].

with satellite radar data (e.g., Nesbitt et al. 2006). Blobs smaller than 10 pixels are too small to determine orientation or aspect ratio, so we analyze these two characteristics only for the 46% of blobs containing at least 10 pixels.

In varying the detection threshold 0–25 dBZ, the cumulative number of detected blobs across the ensemble of trough radar volumes is fairly constant. Aspect ratio, orientation, and reflectivity statistics are insensitive to altering reflectivity thresholds below about 25 dBZ.

Quality control processing of the radar data removes reflectivity data within 15 km of the radar, creating a “center hole” of area  $A_c = 708 \text{ km}^2$  in each scan (e.g., Figs. 4a,b,d,e). About 10% of trough blobs intersect the center hole and the blob algorithm cannot calculate their full areas. The area of each of these blobs is augmented by  $(i/44)A_c$ , where  $i$  is the number of the “perimeter pixels” (44 total) that the blob contains. This changes only the calculated size of the blob.

5) POROSITY WITHIN CONTIGUOUS RAIN AREA BLOBS

It has long been known that holes often exist in MCS rain fields, and this is true near Kwajalein as well (e.g., the dark blob in Fig. 4f, with interior holes of weak reflectivities indicated as white space). We define an MCS with these reflectivity holes to be “porous.” The size and frequency of holes in MCS rain fields is usually unquantified. In MCSs where porosities are large, two-dimensional MCS schematics (e.g., Fig. 1 of Houze et al. 1989) that imply continuous flow within mesoscale circulations may be incomplete representations of the 3D discontinuous air and moisture flow fields. We present a way of quantifying MCS porosity utilizing the blob analysis algorithm and a graphics method. Like the blob detection algorithm, this porosity analysis is objective and may be used in other regions and with model output.

Porosity is defined as areas with reflectivities not exceeding 15 dBZ surrounded by areas with reflectivities above 15 dBZ. To quantify MCS porosity, 1) we identify the perimeter pixels of each MCS across all trough radar volumes (e.g., “chain code,” Russ 1995). Then, 2) the area ( $A$ ) inside the perimeter is calculated as  $A = \frac{1}{2} \sum_{k=1:n-1} [(X_k \cdot Y_{k+1}) - (X_{k+1} \cdot Y_k)]$  (Russ 1995), where  $X$  and  $Y$  are of length  $n$  and contain the  $x$  and  $y$  coordinates of the perimeter pixels, with the first pixel coordinates repeated at the end. Finally, 3) given MCS rain area ( $S$ ), we calculate MCS porosity  $P = 1 - (S/A)$ . As applied here,  $S$  does not contain the correction for the center hole underestimation [section 2b(4)].

Pixel coordinates are defined at the pixel center, so part of each perimeter pixel is excluded in the area

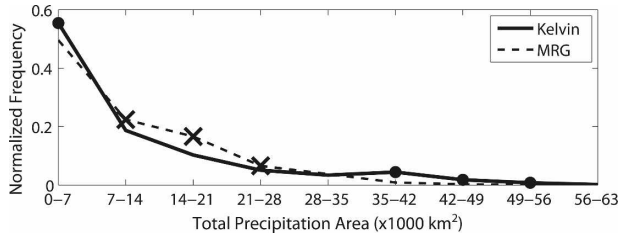


FIG. 5. Normalized frequency of occurrence of total rain areas across trough-centric Kelvin and MRG radar volumes using a reflectivity threshold of 15 dBZ on the 0–2-km altitude layer of radar volumes ( $r = 157 \text{ km}$ ,  $A_d \cong 76\,730 \text{ km}^2$ ). Dots are placed where Kelvin distribution has a significantly greater frequency (to 95% using 10 000-member Monte Carlo test) of that particular rain area bin than MRG, and likewise an X is placed along the MRG line where MRG has a significantly greater frequency than Kelvin.

calculation. Two methods for improving the  $A$  estimation were tested on shapes of known area: (i) subdivide radar pixels to reduce how much of each perimeter pixel is excluded from  $A$ ; (ii) assume that an average of half of each perimeter pixel is excluded from  $A$  and add this estimated missing area to  $A$ . The most computationally efficient method that provided the correct answer was halving the grid spacing, performing steps 1 and 2 (see previous paragraph), and implementing step (ii). Porosity statistics change only slightly if the reflectivity threshold is reduced.

6) EFFECTIVE ECHO HEIGHTS

Radar echo-top data can be used to assess the vigor of precipitating storms. Higher radar echo tops are associated with storms with higher convective available potential energy and stronger updrafts. A robust echo-top statistic must take into account factors such as the non-Gaussian distribution of echo-top height, scan geometry, incomplete beamfilling, and errors in radar calibration. To mitigate these factors, an echo-top height index similar to that of Yuter (2004) is defined corresponding to the lowest layer in the Cartesian interpolated volume below which exists at least 75% of the volume-total precipitation area.

3. Total precipitation area

The total areas of precipitation in the 0–2-km altitude layer for both Kelvin- and MRG-related events had skewed lognormal frequency distributions (Fig. 5). This distribution is common to cloud and radar horizontal size distributions across the tropics (e.g., Houze and Cheng 1977; López 1977; Mapes and Houze 1993) and indicates that total rain areas were usually small—in

TABLE 4. Total precipitation areas ( $\text{km}^2$ ), convective precipitation areas ( $\text{km}^2$ ), and stratiform precipitation areas ( $\text{km}^2$ ) in the trough dataset using the three-dimensional radar volume scans ( $r = 157 \text{ km}$ ,  $A_d \cong 76\,730 \text{ km}^2$ ) and corresponding to percentiles computed from distributions of cumulative frequency.

		Cumulative frequency				Ensemble accumulated area
		25%	50%	75%	90%	
Tot precipitation area	Kelvin	2347	5467	14 235	28 147	37 904 400
	MRG	3191	6967	14 613	21 635	20 150 240
Convective precipitation area	Kelvin	467	1371	3595	5455	8 407 944
	MRG	643	1687	3215	5187	4 612 220
Stratiform precipitation area	Kelvin	1527	3609	10 745	23 376	29 496 456
	MRG	2000	4957	11 465	18 488	15 538 020

this case, most rain areas were less than  $10\,000 \text{ km}^2$  (Table 4). We found a similar distribution when we used the rain event–centric dataset. A similar rain area distribution was also seen in a 1999–2001 Kwajalein radar climatology performed by Yuter et al. (2005) and in a sample of 13 days from the 55-day KWAJEX field experiment (Cetrone and Houze 2006).

Though the precipitation area frequency distributions during Kelvin and MRG waves were generally similar to those typical across the tropics, statistically significant differences existed between Kelvin and MRG trough distributions. Total precipitation areas covering more than 40% of the radar domain ( $>30\,700 \text{ km}^2$ ) occurred with significantly greater frequency during Kelvin trough events compared to MRG (Fig. 5). Significant differences between these Kelvin and MRG trough distributions in the various distribution data bins are calculated to 95% significance using a 10 000-member Monte Carlo significance test. The figure caption explains how significant differences are denoted. Three Kelvin trough events produced rain areas that were larger than those of any MRG event. While we sample more Kelvin trough events than MRG trough events (23 versus 16), this difference is larger than one

would expect due purely to sampling error and suggests that the mesoscale kinematic structures associated with Kelvin troughs tended to be slightly more organized than those of MRG troughs.

#### 4. Visual organization

##### a. Isolated convection

The troughs of both wave types very frequently contained small, isolated convective activity (e.g., Figs. 4a–c). Of the half-hour scans containing precipitation, 53% of trough scans contained only isolated activity (Fig. 3; Table 5). Frequent small, isolated activity is typical near Kwajalein. Using Kwajalein rain gauges, Schumacher and Houze (2000) found that 75% of Kwajalein rain events lasted less than 30 min and accumulated less than 5 mm. Yuter et al. (2005) noted a high frequency of small total rain areas in their Kwajalein radar subset.

Blob analysis of the Kwajalein radar data quantifies the characteristics of contiguous echo regions and may be compared with characteristics in other regions. Using all Kelvin and MRG trough radar volumes, the modal number of blobs per radar scan (radius = 157 km) was between 20 and 50, with a larger mode for

TABLE 5. Statistics on the occurrences and characteristics of the three major horizontal precipitation organizations during our trough events—isolated, MCS, and convective line [see section 2b(3) for organization methodology]. The “both” column considers the Kelvin and MRG datasets together. Frequencies of occurrence were noted visually using convective–stratiform reflectivity maps, calculated from the 0–2-km altitude reflectivity layer of the three-dimensional volume scans ( $r = 157 \text{ km}$ ,  $A_d \cong 76\,730 \text{ km}^2$ ), at 30-min intervals. Sizes and porosities were calculated using the objective blob detection algorithm [section 2b(4)] on all Kelvin and MRG radar volumes.

Organizational statistics		Kelvin	MRG	Both
Isolated cells	% Radar volumes with isolated activity	96%	96%	96%
	% Radar volumes with only isolated activity	54%	49%	53%
	Typical cell size	32 $\text{km}^2$	32 $\text{km}^2$	32 $\text{km}^2$
MCSs	% Radar volumes containing MCSs	21%	20%	21%
	No. of wave events containing MCSs	18 out of 23	14 out of 16	32 of 39
	Median/max MCS size	10 814 $\text{km}^2$ /58 897 $\text{km}^2$	7072 $\text{km}^2$ /39 426 $\text{km}^2$	8776 $\text{km}^2$ /58 897 $\text{km}^2$
	% MCSs with porosity $>0.05$ / $>500 \text{ km}^2$	18%/35%	12%/15%	15%/24%
Convective lines	% Radar volumes with convective lines	7%	2%	6%
	No. of wave events with lines	14 out of 23	3 out of 16	17 of 39

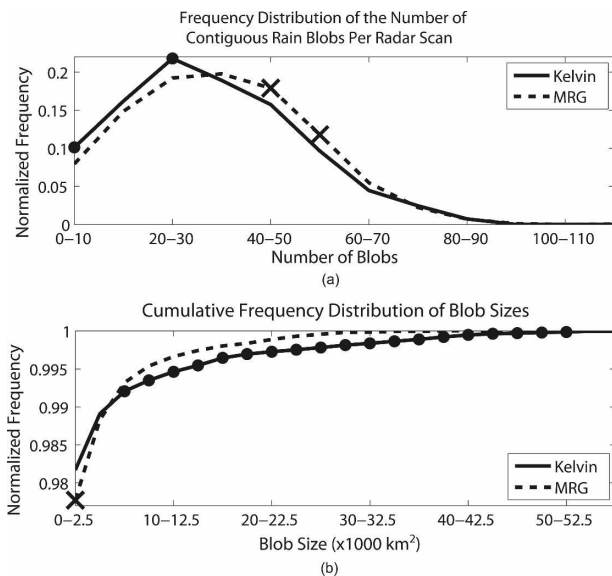


FIG. 6. Normalized frequency of occurrence (a) of the number of blobs per radar scan and (b) of all blob sizes (at the 0–2-km altitude layer of radar volumes,  $r = 157$  km,  $A_d \cong 76\,730$  km<sup>2</sup>) across trough-centric Kelvin and MRG radar volumes using a blob reflectivity threshold of 15 dBZ. Here (b) is plotted as cumulative frequency. The statistical significance is indicated as in Fig. 5.

MRG than Kelvin (Fig. 6a; Table 6). The modal distance between each blob and its closest neighbor was less than 20 km, indicating that blobs were generally closely scattered.

About 73% of blobs had rain areas smaller than 100 km<sup>2</sup> (Fig. 6b), compared to about 61% found by Cetrone and Houze (2006) who used visual rectangular fitting on a subset of data from KWAJEX. This differ-

ence between our study and Cetrone and Houze (2006) may be insignificant given methodology differences. The mean blob length scale in our trough dataset was 25 km, which is larger than the 17-km mean length noted by Nesbitt et al. (2006) over the tropical and subtropical oceans using the Tropical Rainfall Measuring Mission (TRMM) satellite precipitation radar (PR). This difference is likely due to different reflectivity thresholds and spatial scales—15-dBZ 4-km<sup>2</sup> pixel areas in this study compared to the 17–18-dBZ detection threshold and 25-km<sup>2</sup> pixel areas of the TRMM PR.

The ubiquity of small rain blobs indicates that while the regions of convection associated with these wave troughs were by definition synoptically organized as determined using satellite OLR data, the mesoscale precipitation structures within the convective regions were often disorganized as observed with radar data. Visual and blob algorithm analyses do not reveal significant differences between the small, isolated convective structures of Kelvin troughs and those of MRG troughs.

*b. MCS and medium-sized activity*

MCSs are important in Kwajalein rain production. The quantification of the role of MCSs is, not surprisingly, sensitive to the definition of MCS. Nesbitt et al. (2006) follow Houze (1993)’s definition of MCS as cloud systems that occur in connection with an ensemble of thunderstorms and produce a contiguous precipitation area 100 km or more in at least one direction. When Nesbitt et al. (2006) applied this definition to multiyear data from the TRMM PR they found that MCSs are responsible for 50%–60% of rainfall near

TABLE 6. Selected statistics of individual contiguous rain blobs during our trough events using a 15-dBZ reflectivity threshold [section 2b(3)]. Orientation and aspect ratio statistics are only for blobs larger than 10 pixels. “Distance between” is calculated as each blob’s closest neighbor in a given scan (measured between blob centroids). Many reflectivity std dev values were 0.01, so “modal std dev.” is only for the subset of std dev values above 0.01.

Blob statistic		Kelvin	MRG
No. per scan	Frequency distribution	Positively skewed Gaussian	Positively skewed Gaussian
	Mode	28	37
	Max	87	114
Distance between	Frequency distribution	Logarithmic	Logarithmic
	Mode	12 km	12 km
Orientation clockwise from north	Frequency distribution	Nearly nniform	Nearly uniform
Minor:major axis aspect ratio	Frequency distribution	Gaussian	Gaussian
	Mode	0.61	0.58
Reflectivity	Frequency distribution of modal blob value	Logarithmic	Logarithmic
	Modal blob value	16 dBZ	16 dBZ
	Max obs	58 dBZ	62 dBZ
	Modal blob std dev	4 dBZ	4 dBZ
	Max obs std dev	21 dBZ	22 dBZ

Kwajalein. The MCS definition used in this study is similar to that of Rickenbach and Rutledge (1998) and Parker and Johnson (2000) and requires three criteria to be met for a contiguous precipitation area to be considered an MCS—a length scale of at least 100 km, a rain area  $\geq 2500 \text{ km}^2$ , and an aspect ratio  $\geq 0.5$ . Hence, our MCSs represent a subset of those defined with only the 100-km length scale criteria. To illustrate the sensitivity to MCS definition, within Kelvin and MRG troughs, MCSs contribute 37% of cumulative rain area using the three criteria definition and 61% using only the 100-km length scale criteria.

Our category of medium-sized contiguous rain areas is the subset of contiguous rain areas  $\geq 2500 \text{ km}^2$  that do not meet the 100-km length scale criterion. MRG troughs more frequently contained medium-sized blobs than did Kelvin troughs but the larger medium-sized blobs covering at least 20% of the radar domain ( $\geq 15\,350 \text{ km}^2$ ) were more common in Kelvin troughs.

To compare MCS activity among the two wave definitions and outside of defined wave events we use a proxy criterion for MCSs on the long-range scan (240-km radius) two-dimensional dataset. Roughly 75% of the long-range scans containing rain areas larger than  $52\,270 \text{ km}^2$  ( $\sim 28\%$  of long range radar domain) also contained MCSs in the smaller radar volume domain. Using  $52\,270 \text{ km}^2$  as a proxy criterion for MCSs, only 6% of scans during the rainy season achieve MCS status and these contribute 23% of the rainy season cumulative rain area (Table 7). We expect few if any MCSs to occur outside the Kwajalein rainy season. Sixty-five percent of the rain area at Kwajalein is from precipitation structures that combine to yield radar echo between 28% and 55% of the 240-km radius radar domain at any one time (Table 7). The role of these “in between” areas emphasizes the importance of having similar definitions for MCSs when comparing among studies.

Combining the trough-centric and rain event-centric wave definitions, about half of Kwajalein MCSs are associated with Kelvin or MRG waves (Table 7). We have not attempted to determine the large-scale dynamical settings in which the rest of the Kwajalein MCSs occur. Neither tropical cyclones nor the Madden-Julian oscillation are prominent in this region. In the language of the spectral analysis that has become common since Wheeler and Kiladis (1999), it may be that these events are part of the “red noise background.” Although MCSs represent a small absolute percentage of the entire dataset, there were 32 independent MCS events sampled over three years (trough centric: 18 Kelvin, 14 MRG; Tables 5 and 6, 7).

Overall, the frequency of radar volumes containing

TABLE 7. Contribution of MCSs (long-range scan rain areas  $\geq 52\,270 \text{ km}^2$ ), isolated activity (long-range scan rain areas  $< 10\,000 \text{ km}^2$ ), and activity in between these area sizes during the 1999–2003 rainy seasons. Contributions are further broken into subcategories for trough event-centric wave events, rain event-centric wave events, the union of these two categories, and the scans corresponding to neither Kelvin nor MRG activity by either definition.

Tot cumulative area	$1.47 \times 10^9 \text{ km}^2$
Tot contribution of MCSs	23%
Contribution of MCSs in combined trough and rain event-centric dataset	10%
Contribution of MCSs in our trough event-centric dataset	2%
Contribution of MCSs in the S06 rain event-centric dataset	9%
Contribution of MCSs not in Kelvin or MRG events by either definition	12%
Tot contribution of rain areas in between isolated and MCS	65%
Tot contribution of isolated rain areas	12%
Tot No. of scans	88 241
Tot contribution of MCSs	6%
Contribution of MCSs in combined trough and rain event-centric dataset	2.5%
Contribution of MCSs in our trough event-centric dataset	0.4%
Contribution of MCSs in the S06 rain event-centric dataset	2.3%
Contribution of MCSs not in Kelvin or MRG events by either definition	3.5%
Tot contribution of rain areas in between isolated and MCS	45%
Tot contribution of isolated rain areas	49%

MCSs was similar between the Kelvin and MRG datasets (Table 5), but MCS occurrence varied widely from one trough event to the next (Fig. 3). Seven trough events contained no MCS activity, while 61% of scans in one Kelvin event contained MCS activity (Fig. 3). Kelvin MCSs were often larger than MRG MCSs.

While satellite data show that MRG and Kelvin troughs are coupled with large and often contiguous areas of anomalously cold clouds, mesoscale radar data reveal that they are not always associated with large contiguous precipitation areas. At least two of the possible reasons for this are linked to our definition of trough events. First, the widely used Wheeler and Kiladis (1999) spectral analysis method uses twice-daily OLR data, and cloudiness may be discontinuous between these times. Second, we look for strong wave-filtered negative OLR anomalies averaged across a spatial domain to identify strong trough convective activity. During five trough events (Kelvin event numbers 8, 13, and 14; MRG events 7 and 13; Fig. 3), the strongest raw and wave-filtered OLR anomalies were situated outside the Kwajalein radar domain. These five events

had rain areas observed by the Kwajalein radar that were generally smaller than most other wave events, and three events contained only isolated activity. We retain these events in our dataset to minimize subjectivity and remain consistent with how many previous studies identified wave activity. Kelvin and MRG waves may also not be providing enough large-scale forcing consistently across the trough region to sustain MCSs. Other significant forcings, such as other equatorial waves, the diurnal signal, and gravity waves from nearby MCSs (e.g., Mapes 1993; Madden and Julian 1994; Chen and Houze 1997), likely modulate convection near Kwajalein and help produce rain events that often contain isolated blobs. It is also likely that the interaction of waves with convection generates MCSs that, because of their own dynamics such as cold pools, move at different velocities than the wave. MCSs can then decouple from the wave trough and move quasi-independently. This was the view of S06 that led to the rain event–centric approach.

#### MCS EMBEDDED CONVECTION AND POROSITY

MCSs near Kwajalein were often visibly disorganized and contained many embedded convective cores throughout their stratiform region. A visual browsing of TOGA COARE data (Yuter et al. 1995) revealed similar disorganization in west Pacific warm pool MCSs. Many Kwajalein and TOGA COARE MCSs also contained noticeable areas of weak reflectivity, or “pores,” surrounded by convective or stratiform reflectivities [section 2b(5)]. MCS porosity did not correlate well with MCS rain area (Fig. 7).

The relation between porosity and MCS area is complex (Fig. 7). The distribution of porosities is strongly skewed to smaller fractions for contiguous MCS rain areas  $<30\,000\text{ km}^2$  and the largest porosities occurred in a midsize Kelvin MCS ( $12\,515\text{-km}^2$  cumulative pore area, 0.29 porosity fraction). Porosity as small as 0.05 (5%) within an MCS covering  $10\,000\text{-km}^2$  amounts to a  $500\text{-km}^2$  cumulative pore area. This may be large enough to warrant consideration of the physics that lead to these holes. Of all Kelvin blobs identified as MCSs, 32% had pore areas of at least  $500\text{ km}^2$ , compared to 14% of MRG MCSs. As a point of comparison, 92% of contiguous radar echo blobs in our analysis had rain areas smaller than  $500\text{ km}^2$ .

While pores within MCS stratiform precipitation fields are known to exist, this objective method is perhaps the first attempt to quantify pore size and reveals that the pores within Kwajalein MCSs may be large enough to have important dynamical and thermodynamical implications. The idealized schematic in Fig. 8a [based on Fig. 1c from Leary and Houze (1979)] during

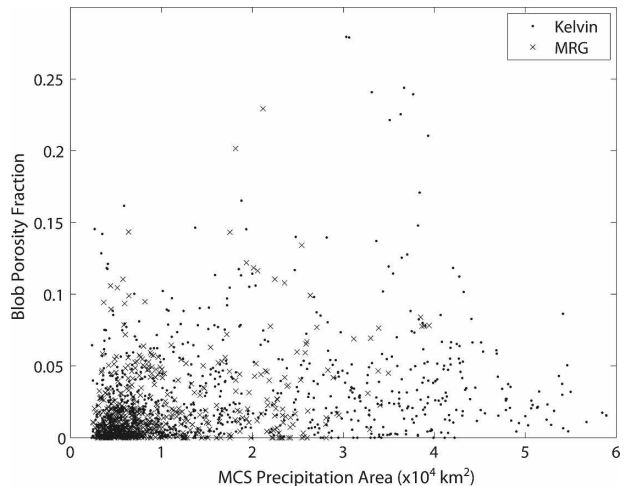


FIG. 7. Observed MCS rain area and corresponding MCS porosity fraction, using a 15-dBZ reflectivity blob detection threshold on the 0–2-km altitude layer of radar volumes ( $r = 157\text{ km}$ ,  $A_d \cong 76\,730\text{ km}^2$ ), for trough-centric Kelvin radar volumes (dot) and MRG radar volumes (x). Zero porosity indicates that the MCS had no embedded areas with reflectivity  $<15\text{ dBZ}$ .

the Global Atmospheric Research Program (GARP) Atlantic Tropical Experiment (GATE)], shows a leading convective line seeding an expansive trailing stratiform area. At Kwajalein, the seeding is not spatially continuous; instead, there are typically many small, embedded convective areas whose collective impact fails to thoroughly seed the entire cloudy region, as shown in Fig. 8b. The stratiform CFADs of our trough event–centric dataset (Figs. 9a,b) and of the S06 rain event–centric dataset (Figs. 9c,d) are generally upright, indicating little to no new hydrometeor growth in the ice layer of the stratiform precipitation regions. This contrasts with much more active vapor deposition and aggregation processes in, for example, an active Kansas–Oklahoma case shown in Fig. 8a of Yuter and Houze (1995).

#### c. Convective lines

Convective lines were infrequent during trough events. For all radar scans, the frequency distribution of blob aspect ratio was Gaussian with a mean near 0.6, meaning the average blob was about 1.7 times longer than it was wide (Table 6). Cetrone and Houze (2006) determined Kwajalein aspect ratios using only the contiguous reflectivity areas in their dataset that were sufficiently elongated to visually determine orientation—those echo areas with aspect ratios less than 0.66, which constituted 83% of their echo areas compared to about 43% of our trough blobs. Using this aspect ratio threshold, Cetrone and Houze (2006) found an average aspect

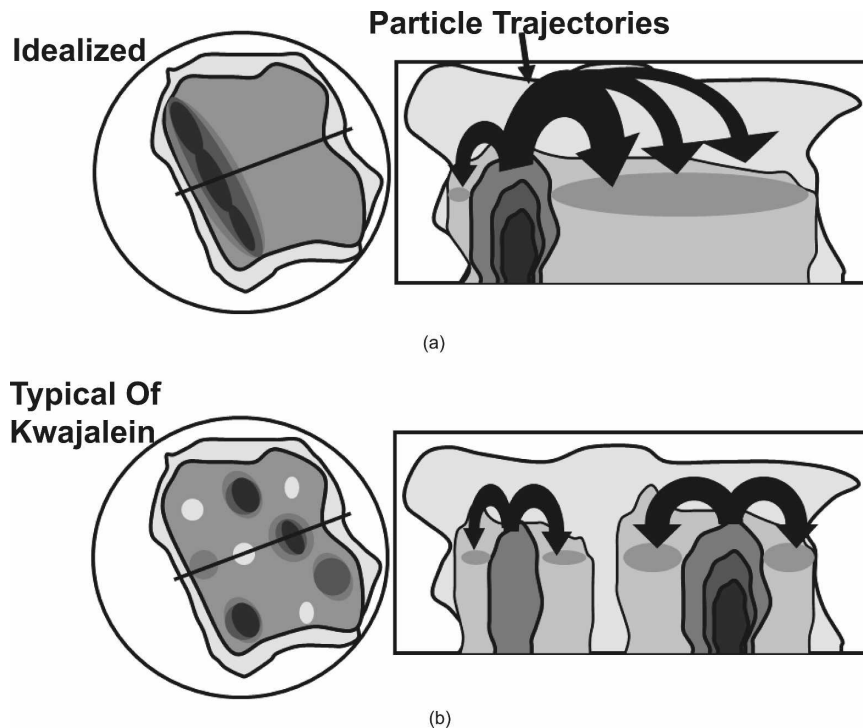


FIG. 8. Schematic representation, with a radar reflectivity plan view and vertical cross section of (a) an idealized mature-stage leading-line trailing-stratiform MCS (based on Fig. 1c of Leary and Houze 1979), and (b) an MCS more typical of Kwajalein and the west Pacific warm pool. The outside contour represents the weakest detectable radar reflectivity, and successive inner contours and shadings represent successively stronger reflectivities. Dark arrows represent hydrometeor particle trajectories emanating from the convective region(s).

ratio of 0.41 for their echo areas, compared to an average near 0.5 for our trough blobs using the same threshold.

Using visual classification [see section 2b(2) for definitions], 7% of Kelvin scans had convective lines, compared to only 2% of MRG scans, amounting to 18 individual lines during Kelvin events and 3 during MRG events. The higher frequency of convective lines during Kelvin events than MRG provides further evidence that the mesoscale precipitation structures in our Kelvin troughs were frequently slightly more organized than those of MRG. Lines were typically less than 150 km long and existed an average of about 2 h within the radar domain (radius = 157 km).

##### 5. Convective and stratiform precipitation structures

Total rain area and stratiform area were, as expected, highly correlated (Fig. 10). Since Kelvin trough rain areas tended to be larger than those of MRG, Kelvin trough stratiform areas tended to be larger (Table 4). In the S06 rain event-centric dataset, Kelvin stratiform

areas tended to be larger than MRG stratiform areas, but the difference was smaller than with our trough dataset—7% of S06 Kelvin stratiform areas and 6% of S06 MRG stratiform areas exceeded 33% of the radar domain ( $\sim 25\,320\text{ km}^2$ ), compared to 8% and 4%, respectively, for our study. This confirms the suggestion in S06 that Kelvin-associated rain areas tend to have larger stratiform rain areas than those of MRG.

The proportion of total precipitation area that is stratiform is called “stratiform area fraction.” Stratiform precipitation contributed 0.77 of the accumulated rain area in both the trough event-centric dataset and in the S06 rain event-centric dataset, and stratiform and weak reflectivities together contributed 0.82. Given that this typical stratiform area fraction value is similar between wave types, it likely reflects typical stratiform area fractions near Kwajalein. Schumacher and Houze (2000), using all radar volumes during August 1998–August 1999, found that stratiform area made up 0.86 of the total accumulated rain area near Kwajalein. This discrepancy with our results is likely due to their requirement of “significant” precipitation. As a point of comparison, the stratiform area proportion of accumu-

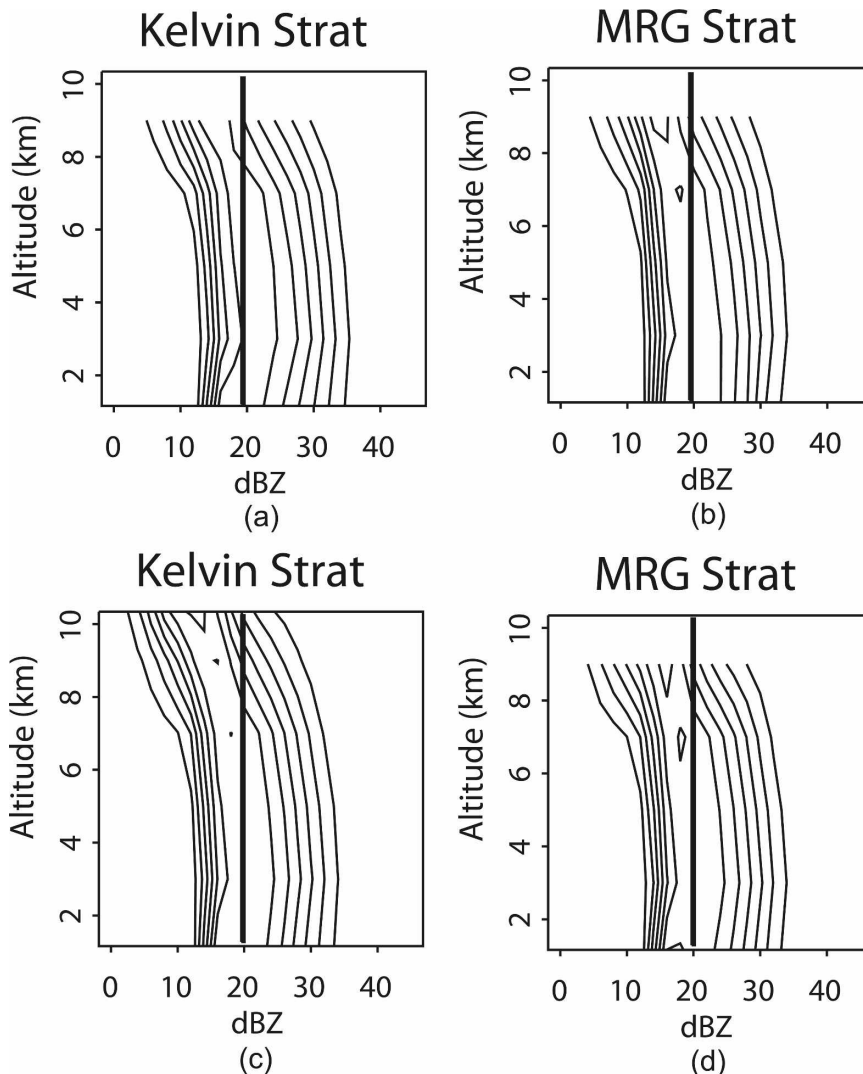


FIG. 9. Accumulated CFADs of stratiform precipitation reflectivity for (a), (b) trough-centric Kelvin and MRG radar volumes and (c), (d) the S06 rain event-centric Kelvin and MRG radar volumes. CFADs are composed for reflectivities  $-15$  to  $60$  dBZ, every  $1$  dB, with contour intervals of  $0.125\%$  data  $\text{dBZ}^{-1} \text{km}^{-1}$ . Vertical lines are drawn to approximate the near-surface modal ensemble stratiform reflectivities.

lated total areas in this study (0.77) is very similar to observations during the East Pacific Investigation of Climate Processes in the Coupled Ocean-Atmosphere System (0.76; Cifelli et al. 2007), less than during the Tropical Eastern Pacific Process Study (TEPPS; 0.84; Cifelli et al. 2007), and more than during TOGA COARE ship cruises (0.66–0.74; Short et al. 1997). These differences in stratiform area fraction may not be significant given differences in methodology among these studies.

The distributions of stratiform precipitation area fraction and of convective precipitation area reveal features that are similar across the western tropical Pacific.

The stratiform area fractions near Kwajalein (Fig. 11) show a distinct pattern that was also observed in the west Pacific warm pool during TOGA COARE (Yuter and Houze 1998, their Fig. 24). For small rain areas, stratiform rain fractions have wide variability. As total rain area increases, the variance of stratiform area fractions decreases and the minimum stratiform area fraction for a given total precipitation area converges to 1.0. This relation is refined by the larger sample size in this study compared to Yuter and Houze (1998) and yields a well-defined separation between observed and unobserved stratiform area fractions for a given total rain area. The similarity of results between TOGA COARE and

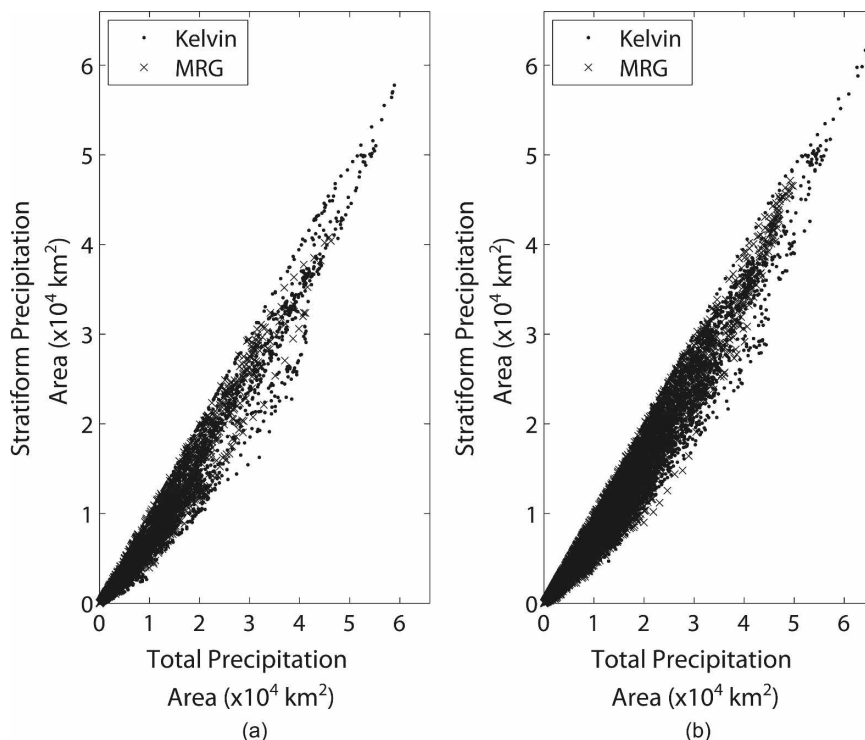


FIG. 10. Scatterplot of observed stratiform rain area per total rain area across all Kelvin and MRG radar volumes in (a) the trough-centric dataset and in (b) the S06 rain event-centric dataset. Total area and stratiform area are calculated on the 0–2-km altitude layer of radar volumes ( $r = 157$  km,  $A_d \cong 76\,730$  km<sup>2</sup>).

the long term dataset at Kwajalein implies that the results may have applicability to other tropical oceanic areas.

Also consistent with findings from TOGA COARE (Yuter and Houze 1998, their Fig. 23), convective precipitation area was not well correlated with total rain area (Fig. 12). There is also a well-defined separation between observed and unobserved convective areas as a function of total precipitation area covering less than about 40% of the radar domain ( $<30\,700$  km<sup>2</sup>). For trough radar volumes with total rain areas exceeding  $33\,000$  km<sup>2</sup>, the maximum observed convective area decreased as a function of total area. This increasing then decreasing relation between convective area and increasing precipitation area is very similar between the trough event-centric dataset and rain event-centric dataset (not shown). The distributions of convective precipitation area were very similar between the Kelvin and MRG wave types (Table 4).

Convective precipitation areas did not exceed 20% ( $15\,684$  km<sup>2</sup>) of the radar domain, which is similar to aircraft observations during TOGA COARE (Yuter and Houze 1998). The maximum observed convective area, which may represent an approximate limit on convective precipitation area near Kwajalein, occurred in a

Kelvin trough event within a total rain area of about  $33\,000$  km<sup>2</sup> (43% of the radar domain). The maximum observed MRG trough convective area was nearly  $5000$  km<sup>2</sup> smaller than that within a Kelvin trough.

A tendency for slightly larger total convective areas and total precipitation areas during Kelvin trough events than MRG events is supported by results from Wheeler et al. (2000). Through a 17-yr composite of reanalysis data, their Figs. 7 and 15 suggest that convectively coupled Kelvin waves are associated with deeper and perhaps stronger updrafts, and thus more enhanced convergence through the tropospheric column, than those of MRG waves. The updraft region also appears to be more persistent in time with respect to the wave-filtering base point.

The Kwajalein radar dataset and the TOGA COARE aircraft dataset indicate a similar convective precipitation area limit as a function of the observed domain. These characteristics imply limits on processes that initiate and sustain updrafts of sufficient magnitude and moisture content to support precipitation growth by collision/coalescence and riming. The physical reasons for this apparent limit on convective precipitation area should be a subject of future research.

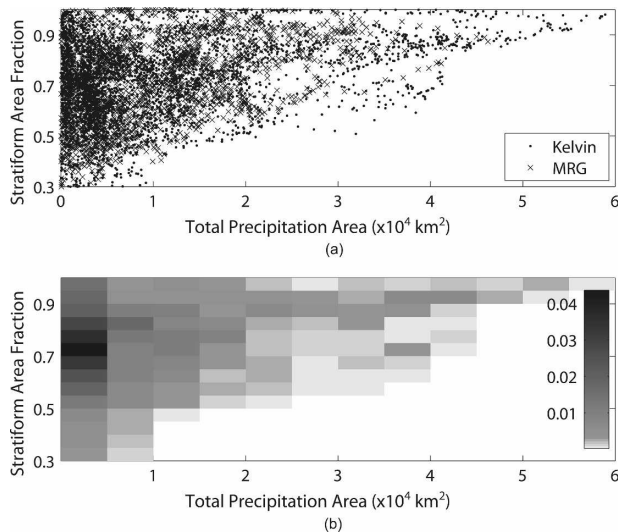


FIG. 11. Observed stratiform rain area fractions per total rain area for trough-centric Kelvin and MRG radar volumes: (a) is a scatterplot version, and to more clearly indicate the frequency distribution, (b) is a density plot representation of (a) where darker shadings indicate higher frequencies. Stratiform area fraction is calculated on the 0–2-km altitude layer of radar volumes ( $r = 157$  km,  $A_d \cong 76\,730$  km<sup>2</sup>). Stratiform fractions below 0.3 are infrequent and omitted. Note that there are no stratiform area fractions for MRG for total rain areas  $>46\,224$  km<sup>2</sup> because such total areas were not observed for MRG cases.

**6. Echo-top height index**

Most precipitating clouds at Kwajalein are mixed phase. The freezing level height is near 4.8-km altitude (Yuter et al. 2005) and the modal echo-top height index in our trough dataset was near 7-km altitude (Fig. 13). Kelvin and MRG troughs had nearly identical frequency distributions of echo heights for convective and stratiform reflectivity subsets. Here, similar to Yuter (2004) results during TEPPS (Yuter and Houze 2000; Yuter et al. 2000) and TOGA COARE, the variance in convective and stratiform heights decreased with increasing convective and stratiform area. Total rain areas larger than 10 000 km<sup>2</sup> always had echo heights above 5-km altitude. Data from GATE (Houze and Cheng 1977) and from 13 sampled days during KWAJEX (Cetrone and Houze 2006) contained a positive but scattered relationship between rain area and echo height, which was not found here.

**7. Conclusions**

This study builds on the work of Swann et al. (2006) and is among the first to use a multiyear dataset of three-dimensional ground-based radar data to analyze the characteristics of precipitation structures associated

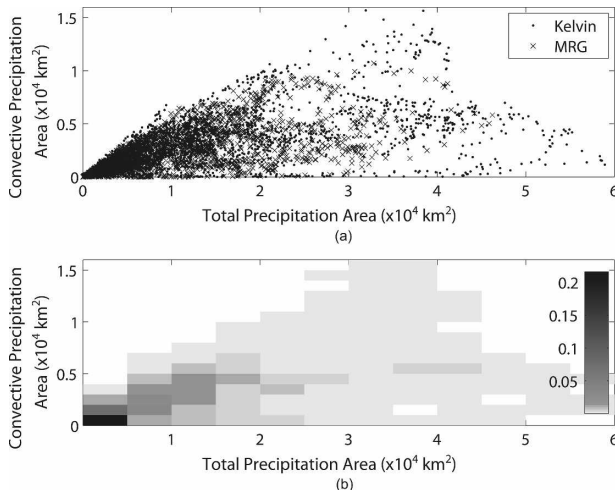


FIG. 12. As in Fig. 11, but with observed convective precipitation areas per total rain area. Convective rain areas  $>10\,716$  km<sup>2</sup> only occur in the Kelvin data. These large convective areas are reached and sustained during two Kelvin wave events.

with equatorial waves over the tropical open ocean. Previous studies of open-ocean equatorial wave characteristics using shipborne and airborne radar data were limited by the few-week duration of aircraft and ship deployments (e.g., Houze et al. 2000; Serra and Houze 2002; Petersen et al. 2003). We use several analytical techniques to describe the structures within 23 Kelvin and 16 MRG troughs. MCSs were identified during portions of 32 of the 39 wave trough events examined. We also utilize the  $\sim 800$ -day 3-yr rainy season long-range two-dimensional radar dataset from Yuter et al. (2005) to describe the overall Kwajalein climatology and to compare to the wave event subsets. In contrast to the snapshots provided every few days over a given location by TRMM PR (e.g., Morita et al. 2006; Nesbitt et al. 2006), ground-based radar provides five to six samples per hour while the feature of interest remains within the radar domain.

Consistent with the results of Reed and Recker (1971) for the Marshall Islands region, wave troughs are preferred locations for precipitation and at Kwajalein typically yield 1.3 times more rain area than the overall rainy season climatology. However, nearly half of the radar volumes in our trough dataset consisted only of small, isolated precipitation areas (Table 5). Thus, while satellite data show that MRG and Kelvin troughs are coupled with large areas of anomalously cold clouds, mesoscale radar data indicate they are not always associated with large contiguous precipitation areas.

Combining the trough-centric and rain-centric definitions, Kelvin and MRG wave events account for 30%

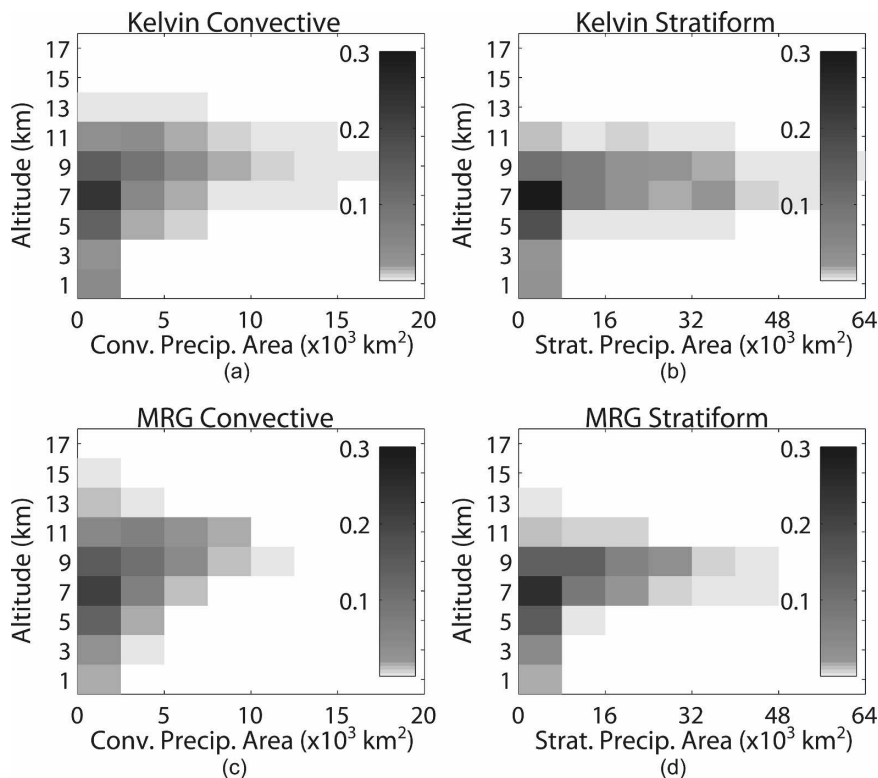


FIG. 13. Density plots of the normalized frequency distribution of echo height indices for (a), (b) trough-centric Kelvin and (c), (d) MRG (a), (c) convective and (b), (d) stratiform precipitation areas. Darker shadings represent higher frequencies, and the same shading scale is used on each plot. Altitude bins are centered on each 2-km layer of radar data (e.g., the 1-km bin represents the 0–2-km altitude layer).

of the cumulative rain area and half of MCSs observed near Kwajalein. We found only slight differences between precipitation structures within Kelvin and MRG waves. Despite being based on nearly disjoint subsets (section 2a), both the trough-centric and S06's rain-centric definitions of Kelvin and MRG waves yielded similar statistics across several objective measures, including two-dimensional convective and stratiform areas and three-dimensional CFADs and echo-top heights (sections 4, 5, and 6). The observed differences in precipitation structure between wave types were primarily associated with larger, MCS-scale precipitation areas. Compared to MRG troughs, Kelvin troughs had larger contiguous MCS radar echoes and larger 90th percentile and maximum total precipitation and stratiform precipitation areas (Table 4; Figs. 5, 6, and 10). This conclusion is consistent with the speculation of S06 based on a CFAD analysis of the total reflectivity distribution. Larger MCSs and rain areas suggest that Kelvin trough MCSs near Kwajalein often contain more organized mesoscale circulations than MCSs within MRG troughs. Another difference between the

wave types was that the distribution of the magnitude of vertical wind shear was biased slightly higher in Kelvin compared to MRG trough events (Fig. 2).

Convective lines were much more common in Kelvin troughs than MRG troughs (Fig. 3; Table 5). The leading-line trailing-stratiform MCS structure was infrequent near Kwajalein. Rather, typical Kwajalein MCSs have embedded convective cells and areas of weak reflectivity (pores) throughout the stratiform region (Figs. 4 and 8b). Inhomogeneities in the horizontal stratiform reflectivity field exist in many global locations. We present a method of quantifying MCS porosity that can be applied to other datasets. Porosity was usually <5% of blob precipitation area but can be as large as 25%. When pores occupy a large portion of the radar echo area, these “holes” in the stratiform structure may interrupt mesoscale circulations.

Similar to the west Pacific warm pool region, there is a well-defined separation between observed and unobserved stratiform area fraction as a function of total precipitation area (Fig. 11). Convective precipitation area also exhibits a distinct pattern as a function of total

precipitation area (Fig. 12). At precipitation area sizes near 40% of the radar domain, the maximum observed convective area changes from increasing to decreasing with increasing precipitation area. The maximum observed convective precipitation area occupied  $\sim 20\%$  of the radar domain. These characteristics suggest that the atmosphere in the west Pacific can sustain a limited area of updrafts capable of supporting precipitation growth by collision/coalescence and riming. Precipitation areas larger than 40% of the radar domain primarily increase in size by increasing the stratiform precipitation area.

The generality of our findings with these and other types of waves should be investigated for other tropical regions where long-term radar datasets exist. Objective blob analysis may be useful in quantifying the horizontal characteristics of individual rain areas in other regions and in model output, while the volume-wide echo height index may be a more useful representation of storm heights than following particular reflectivity contours, particularly for surface-based scanning radar. The results of many of the statistical analyses of precipitation structures that we employ, especially the ensemble thresholds of convective and stratiform precipitation structures, would be convenient to compare to model output. It may be useful to quantify MCS embedded convection and MCS porosity in other regions, to study their physical implications, and to evaluate the realism of modeled MCSs.

*Acknowledgments.* George Kiladis (NOAA) provided the OLR dataset and Peter Blossey (University of Washington) provided the blob detection script and assisted with it. Thanks to Catherine Spooner, Kimberly Comstock, Matthew Miller, Steve Nesbitt, John Russ, Fredrick Semazzi, and Matthew Parker for their help. This study was supported by a North Carolina Space Grant Fellowship, NASA Grants NN604GA65G and NNX07AD21G, and NSF Grant ATM-0544766.

#### REFERENCES

- Cetrone, J., and R. A. Houze, 2006: Characteristics of tropical convection over the ocean near Kwajalein. *Mon. Wea. Rev.*, **134**, 834–853.
- Chen, S. S., and R. A. Houze, 1997: Diurnal variation and life-cycle of deep convective systems over the tropical Pacific warm pool. *Quart. J. Roy. Meteor. Soc.*, **123**, 357–388.
- Cifelli, R., S. W. Nesbitt, S. A. Rutledge, W. A. Petersen, and S. Yuter, 2007: Radar characteristics of precipitation features in the EPIC and TEPPS regions of the east Pacific. *Mon. Wea. Rev.*, **135**, 1576–1595.
- Dunkerton, T. J., 1993: Observation of 3–6-day meridional wind oscillations over the tropical Pacific, 1973–1992: Vertical structure and interannual variability. *J. Atmos. Sci.*, **50**, 3292–3307.
- , and M. P. Baldwin, 1995: Observation of 3–6-day meridional wind oscillations over the tropical Pacific, 1973–1992: Horizontal structure and propagation. *J. Atmos. Sci.*, **52**, 1585–1601.
- Grabowski, W. W., 2003: MJO-like coherent structures: Sensitivity simulations using the cloud-resolving convective parameterization (CRCP). *J. Atmos. Sci.*, **60**, 847–864.
- , 2004: An improved framework for superparameterization. *J. Atmos. Sci.*, **61**, 1940–1952.
- Hendon, H. H., and B. Liebmann, 1991: The structure and annual variation of antisymmetric fluctuations of tropical convection and their association with Rossby–gravity waves. *J. Atmos. Sci.*, **48**, 2127–2140.
- Houze, R. A., 1993: *Cloud Dynamics*. Academic Press, 573 pp.
- , 2004: Mesoscale convective systems. *Rev. Geophys.*, **42**, RG4003, doi:10.1029/2004RG000150.
- , and C. Cheng, 1977: Radar characteristics of tropical convection observed during GATE: Mean properties and trends over the summer season. *Mon. Wea. Rev.*, **105**, 964–980.
- , S. A. Rutledge, M. I. Biggerstaff, and B. F. Smull, 1989: Interpretation of Doppler weather-radar displays in midlatitude mesoscale convective systems. *Bull. Amer. Meteor. Soc.*, **70**, 608–619.
- , S. S. Chen, D. E. Kingsmill, Y. Serra, and S. E. Yuter, 2000: Convection over the Pacific warm pool in relation to the atmospheric Kelvin–Rossby wave. *J. Atmos. Sci.*, **57**, 3058–3089.
- , S. Brodzik, C. Schumacher, S. E. Yuter, and C. R. Williams, 2004: Uncertainties in oceanic radar rain maps at Kwajalein and implications for satellite validation. *J. Appl. Meteor.*, **43**, 1114–1132.
- Khairoutdinov, M., D. Randall, and C. DeMott, 2005: Simulations of the atmospheric general circulation using a cloud-resolving model as a superparameterization of physical processes. *J. Atmos. Sci.*, **62**, 2136–2154.
- Kuang, Z., P. N. Blossey, and C. S. Bretherton, 2005: A new approach for 3D cloud-resolving simulations of large-scale atmospheric circulation. *Geophys. Res. Lett.*, **32**, L02809, doi:10.1029/2004GL021024.
- Leary, C. A., and R. A. Houze, 1979: The structure and evolution of convection in a tropical cloud cluster. *J. Atmos. Sci.*, **36**, 437–457.
- Liebmann, B., and C. A. Smith, 1996: Description of a complete (interpolated) outgoing longwave radiation dataset. *Bull. Amer. Meteor. Soc.*, **77**, 1275–1277.
- Lindzen, R. S., 1967: Planetary waves on beta planes. *Mon. Wea. Rev.*, **95**, 441–451.
- , and T. Matsuno, 1968: On the nature of large-scale wave disturbances in the equatorial lower stratosphere. *J. Meteor. Soc. Japan*, **46**, 215–221.
- López, R. E., 1977: The lognormal distribution and cumulus cloud populations. *Mon. Wea. Rev.*, **105**, 865–872.
- Madden, R. A., and P. R. Julian, 1994: Observations of the 40–50-day tropical oscillation—A review. *Mon. Wea. Rev.*, **122**, 814–837.
- Majda, A. J., B. Khouider, G. N. Kiladis, K. H. Straub, and M. G. Shefter, 2004: A model for convectively coupled tropical waves: Nonlinearity, rotation, and comparison with observations. *J. Atmos. Sci.*, **61**, 2188–2205.
- Mapes, B. E., 1993: Gregarious tropical convection. *J. Atmos. Sci.*, **50**, 2026–2037.
- , and R. A. Houze, 1993: Cloud clusters and superclusters over the oceanic warm pool. *Mon. Wea. Rev.*, **121**, 1398–1416.

- Matsuno, T., 1966: Quasi-geostrophic motions in the equatorial area. *J. Meteor. Soc. Japan*, **44**, 25–43.
- Medioni, G., M. S. Lee, and C. K. Tang, 2000: *A Computational Framework for Segmentation and Grouping*. Elsevier, 260 pp.
- Morita, J., Y. N. Takayabu, S. Shige, and Y. Kodama, 2006: Analysis of rainfall characteristics of the Madden-Julian oscillation using TRMM satellite data. *Dyn. Atmos. Oceans*, **42**, 107–126.
- Nesbitt, S. W., E. J. Zipser, and D. J. Cecil, 2000: A census of precipitation features in the tropics using TRMM: Radar, ice scattering, and lightning observations. *J. Climate*, **13**, 4087–4106.
- , R. Cifelli, and S. A. Rutledge, 2006: Storm morphology and rainfall characteristics of TRMM precipitation features. *Mon. Wea. Rev.*, **134**, 2702–2721.
- Parker, M. D., and R. H. Johnson, 2000: Organizational modes of midlatitude mesoscale convective systems. *Mon. Wea. Rev.*, **128**, 3413–3436.
- Petersen, W. A., R. Cifelli, D. J. Boccippio, S. A. Rutledge, and C. Fairall, 2003: Convection and easterly wave structures observed in the eastern Pacific warm pool during EPIC-2001. *J. Atmos. Sci.*, **60**, 1754–1773.
- Pires, P., J. L. Redelsperger, and J. P. Lafore, 1997: Equatorial atmospheric waves and their association to convection. *Mon. Wea. Rev.*, **125**, 1167–1184.
- Randall, D., M. Khairoutdinov, A. Arakawa, and W. Grabowski, 2003: Breaking the cloud parameterization deadlock. *Bull. Amer. Meteor. Soc.*, **84**, 1547–1564.
- Reed, R. J., and E. E. Recker, 1971: Structure and properties of synoptic-scale wave disturbances in the equatorial western Pacific. *J. Atmos. Sci.*, **28**, 1117–1133.
- Rickenbach, T. M., and S. A. Rutledge, 1998: Convection in TOGA COARE: Horizontal scale, morphology, and rainfall production. *J. Atmos. Sci.*, **55**, 2715–2729.
- Roundy, P. E., and W. M. Frank, 2004: A climatology of waves in the equatorial region. *J. Atmos. Sci.*, **61**, 2105–2132.
- Russ, J. C., 1995: *The Image Processing Handbook*. CRC Press, 674 pp.
- Schumacher, C., and R. A. Houze, 2000: Comparison of radar data from the TRMM satellite and Kwajalein oceanic validation site. *J. Appl. Meteor.*, **39**, 2151–2164.
- Serra, Y. L., and R. A. Houze, 2002: Observations of variability on synoptic timescales in the east Pacific ITCZ. *J. Atmos. Sci.*, **59**, 1723–1743.
- Short, D. A., P. A. Kucera, B. S. Ferrier, J. C. Gerlach, S. A. Rutledge, and O. W. Thiele, 1997: Shipboard radar rainfall patterns within the TOGA COARE IFA. *Bull. Amer. Meteor. Soc.*, **78**, 2817–2836.
- Slingo, J., P. Inness, J. Strachan, S. Woolnough, and G. Y. Yang, 2007: Systematic errors in the tropics and the role of multi-scale interactions. Abstracts, *Third WGN Workshop on Systematic Errors in Climate and NWP Models*, San Francisco, CA, Program for Climate Model Diagnosis and Intercomparison, Lawrence Livermore National Laboratory, 101.
- Sobel, A. H., S. E. Yuter, C. S. Bretherton, and G. N. Kiladis, 2004: Large-scale meteorology and deep convection during TRMM KWAJEX. *Mon. Wea. Rev.*, **132**, 422–444.
- Steiner, M., R. A. Houze, and S. E. Yuter, 1995: Climatological characterization of three-dimensional storm structure from operational radar and rain gauge data. *J. Appl. Meteor.*, **34**, 1978–2007.
- Straub, K. H., and G. N. Kiladis, 2002: Observations of a convectively coupled Kelvin wave in the eastern Pacific ITCZ. *J. Atmos. Sci.*, **59**, 30–53.
- , and —, 2003a: Extratropical forcing of convectively coupled Kelvin waves during austral winter. *J. Atmos. Sci.*, **60**, 526–543.
- , and —, 2003b: The observed structure of convectively coupled Kelvin waves: Comparison with simple models of coupled wave instability. *J. Atmos. Sci.*, **60**, 1655–1668.
- Suzuki, T., Y. N. Takayabu, and S. Emori, 2006: Coupling mechanisms between equatorial waves and cumulus convection in an AGCM. *Dyn. Atmos. Oceans*, **42**, 81–106.
- Swann, A., A. H. Sobel, S. E. Yuter, and G. N. Kiladis, 2006: Observed radar reflectivity in convectively coupled Kelvin and mixed Rossby-gravity waves. *Geophys. Res. Lett.*, **33**, L10804, doi:10.1029/2006GL025979.
- Webster, P., and R. Lukas, 1992: TOGA COARE: The Coupled Ocean–Atmosphere Response Experiment. *Bull. Amer. Meteor. Soc.*, **73**, 1377–1416.
- Wheeler, M., and G. N. Kiladis, 1999: Convectively coupled equatorial waves: Analysis of clouds and temperature in the wave-number–frequency domain. *J. Atmos. Sci.*, **56**, 374–399.
- , —, and P. J. Webster, 2000: Large-scale dynamical fields associated with convectively coupled equatorial waves. *J. Atmos. Sci.*, **57**, 613–640.
- Yang, G. Y., B. J. Hoskins, and J. M. Slingo, 2007: Convectively coupled equatorial waves in the Hadley Centre climate models. Abstracts, *Third WGN Workshop on Systematic Errors in Climate and NWP Models*, San Francisco, CA, Program for Climate Model Diagnosis and Intercomparison, Lawrence Livermore National Laboratory, 141.
- Yuter, S. E., 2004: The structure and variability of tropical oceanic precipitation in the western Pacific warm pool and eastern Pacific ITCZ. *Third European Conf. on Radar in Meteorology and Hydrology*, Gotland, Sweden, Copernicus GmbH, 99–104.
- , and R. A. Houze, 1995: Three-dimensional kinematic and microphysical evolution of Florida cumulonimbus. Part II: Frequency distributions of vertical velocity, reflectivity, and differential reflectivity. *Mon. Wea. Rev.*, **123**, 1941–1963.
- , and —, 1998: The natural variability of precipitating clouds over the western Pacific warm pool. *Quart. J. Roy. Meteor. Soc.*, **124**, 53–99.
- , and —, 2000: The 1997 Pan American Climate Studies Tropical Eastern Pacific Process Study. Part I: ITCZ region. *Bull. Amer. Meteor. Soc.*, **81**, 451–481.
- , —, B. F. Smull, F. D. Marks, J. R. Daugherty, and S. R. Brodzik, 1995: TOGA COARE aircraft mission summary images: An electronic atlas. *Bull. Amer. Meteor. Soc.*, **76**, 319–328.
- , Y. L. Serra, and R. A. Houze, 2000: The 1997 Pan American Climate Studies Tropical Eastern Pacific Process Study. Part II: Stratocumulus region. *Bull. Amer. Meteor. Soc.*, **81**, 483–490.
- , R. A. Houze, E. A. Smith, T. T. Wilheit, and E. Zipser, 2005: Physical characterization of tropical oceanic convection observed in KWAJEX. *J. Appl. Meteor.*, **44**, 385–415.
- Ziemiański, M. Z., W. W. Grabowski, and M. W. Moncrieff, 2005: Explicit convection over the western Pacific warm pool in the Community Atmospheric Model. *J. Climate*, **18**, 1482–1502.